

Cite this: *Nanoscale Adv.*, 2024, 6, 4071Received 3rd April 2024  
Accepted 28th June 2024

DOI: 10.1039/d4na00281d

rsc.li/nanoscale-advances

# Accelerating the electron-transfer of nitrogen electro-fixation through assembling Fe nanoparticles into Fe nanochains†

Rongkang Wang,<sup>‡\*</sup> Jingyu Lu,<sup>‡\*b</sup> Xu Li<sup>c</sup> and Chunyu Song<sup>a</sup>

Electrochemically synthesizing  $\text{NH}_3$  via  $\text{N}_2$  is a facile and sustainable approach that involves multistep electron and proton transfer processes. Thus, consecutive electron and proton transfer is necessary. Here, a universal method with the assistance of magnetic stirring that can assemble Fe, Co, and Ni nanoparticles into nanochains is developed. Notably, the Fe nanochain, composed of amorphous Fe nanoparticles, facilitates electron and proton transfer, resulting in an enhanced  $\text{NH}_3$  yield ( $92.42 \mu\text{g h}^{-1} \text{mg}^{-1}$ ) and faradaic efficiency (20.02%) at  $-0.4 \text{ V}$  vs. RHE during the electrochemical reduction of  $\text{N}_2$ . This work offers new insight into designing tandem electrocatalysts.

## Introduction

Ammonia ( $\text{NH}_3$ ) is a vital component in many industrial applications, including fertilizers, pharmaceuticals, and refrigerants, underscoring its global significance.<sup>1–4</sup> Currently, the industrial Haber–Bosch process, which is the primary method for producing  $\text{NH}_3$ , typically operates at high temperatures ( $400\text{--}500^\circ\text{C}$ ) and pressures ( $200\text{--}300 \text{ atm}$ ), leading to substantial energy consumption worldwide.<sup>5,6</sup> In recent years, the electrochemical synthesis of  $\text{NH}_3$  from the  $\text{N}_2$  reduction reaction (NRR) has emerged as a promising and sustainable alternative, allowing for the hydrogenation of  $\text{N}_2$  molecules through multistep proton and electron transfers at ambient temperature and pressure.<sup>7–10</sup> In this context, the role of electrocatalysts, particularly those based on transition metals, is of paramount importance. Inspired by natural nitrogenases such as FeMo-

FeV-, and FeFe-found in rhizobium plants, Fe-based electrocatalysts have been extensively studied.<sup>11–13</sup> Various Fe compounds, including Fe oxides and Fe sulfides, have demonstrated excellent performance in the NRR.<sup>14–16</sup>

Amorphous electrocatalysts, due to their high density of exposed active sites, have been extensively explored in the NRR.<sup>17,18</sup> The concept of tandem active sites, which has been successfully applied in several multistep electrocatalytic processes, offers a promising approach.<sup>19–22</sup> These active sites, each possessing distinct adsorption–desorption characteristics and electron transfer capabilities, can be sequentially arranged at the atomic level to enhance electrocatalytic performance.<sup>20</sup> Additionally, the assembly of small particles into different morphologies or pore structures can further facilitate electron and proton transfer.<sup>23</sup> Therefore, the strategic utilization of active sites in amorphous materials and the assembly of tandem electrocatalysts present a potential pathway for the design of electrocatalysts for nitrogen electro-fixation.

Herein, we assemble amorphous Fe nanoparticles into nanochains by a facile magnetic-assisted method. When the Fe nanochain was applied as the electrocatalyst for electrochemical reduction of  $\text{N}_2$ , it takes full advantage of the active sites of amorphous Fe nanoparticles to promote the multistep electron and proton transfer and produce  $\text{NH}_3$ .

## Experimental section

### Materials synthesis

The Fe nanochain was synthesized by the chemical reduction method. In detail, 50 mg  $\text{FeCl}_2$  was dissolved in 30 mL of deionized water. Then 500 mg  $\text{NaBH}_4$  was dosed into the above solution and magnetically stirred at 1600 rpm at room temperature for 2 h. The Fe nanochain precipitates were finally obtained by cleaning with deionized water three times. The Fe nanoparticles were obtained by a similar procedure to Fe nanochains but without magnetic stirring just standing for 2 h.

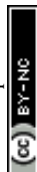
<sup>a</sup>Chongqing Chemical Industry Vocational College, Chongqing, 401228, China. E-mail: wrk1992@163.com

<sup>b</sup>School of Materials Science and Engineering, China University of Petroleum (East China), Qingdao 266580, China

<sup>c</sup>Southwest Technology and Engineering Research Institute, Chongqing 401329, China

† Electronic supplementary information (ESI) available. See DOI: <https://doi.org/10.1039/d4na00281d>

‡ These authors equally contributed to the work.



## Physical characterization

Morphology was observed on a field emission scanning electron microscope (FESEM, JEOL 7800F), transmission electron microscope (TEM), and high-resolution transmission electron microscope (HRTEM, Titan G2 60-300, a spherical and chromatic aberration imaging corrector). The crystal structure was examined by using an X-ray diffractometer (XRD, D8 Advance, Bruker, Karlsruhe, Germany 9 kw, 40 kV, 40 mA,  $\lambda = 1.5418 \text{ \AA}$ ) with Cu-K $\alpha$  radiation. The chemical state was analyzed by X-ray photoelectron spectroscopy (XPS, Thermo ESCALAB 250XI between 0 and 1400 eV). Ultraviolet-visible (UV-vis) absorption spectra were recorded on an Agilent Cary 60.

## Results and discussion

### Synthesis and characterization

The Fe nanochain, assembled *via* magnetic stirring during the chemical reduction process, is composed of Fe nanoparticles. The morphology was visualized using scanning electron microscopy (SEM). As shown in Fig. 1a, the Fe nanochain extends to approximately  $3.1 \mu\text{m}$  in length, and its interwoven structure forms conspicuous nanopores (Fig. 1b). Fig. 1c illustrates the orderly assembly of Fe nanoparticles into the nanochain. In contrast, in the absence of magnetic stirring, the Fe nanoparticles accumulate randomly into agglomerates (Fig. 1d and e). Upon magnification, the individual Fe nanoparticles become clearly visible (Fig. 1f). The STEM elemental mapping of Fe nanochains and Fe nanoparticles respectively demonstrates that Fe is uniformly dispersed in both the nanochains and nanoparticles (Fig. 1g–j).

Transmission Electron Microscopy (TEM) images further corroborate the nanochain morphology of Fe (Fig. 2a and b). Upon magnification of the edge of the Fe nanochain, no lattice fringe is observed. Examination of a single Fe nanoparticle within the nanochain reveals an edge approximately 4 nm thick and a core with a diameter of 23 nm. Within this structure, Fe atoms exhibit a gradual ordering from the edge (Fig. 2e) to the core (Fig. 2d). In addition, no diffraction dots and rings are observed in FFT from the corresponding TEM (Fig. 2f), suggesting its amorphous phase. In agreement with the TEM

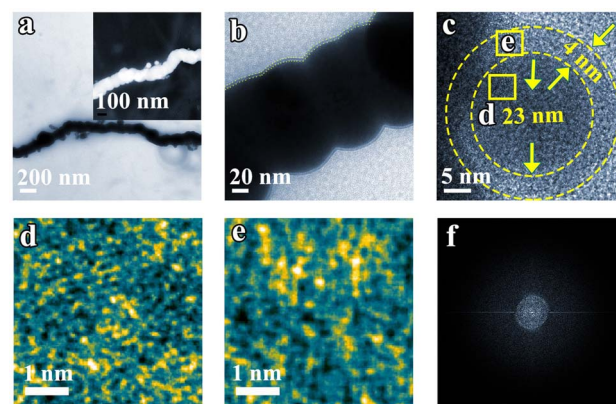


Fig. 2 (a and b) TEM images of Fe nanochains. (c) HRTEM image of the Fe nanochain. (d and e) Selected area magnification HR-TEM from the edge (d) and interior (e). (f) Electron diffraction obtained by Fourier transform.

results, the XRD patterns also show the Fe nanoparticle and nanochain are amorphous (Fig. S1†). This amorphous material may expose a more active site to promote the electrocatalytic NRR. To explore the universality of the synthesized nanochain, magnetic element Co and Ni nano-chains were also prepared by the same method as the Fe nanochain. Fig. S2–S5† show that the Ni and Co nano-chains were successfully obtained which also exhibit their amorphous state.

### Electrocatalytic nitrogen reduction performances

The electrocatalytic  $\text{N}_2$  fixation performances of the amorphous Fe nanochain and nanoparticle were evaluated. First, linear sweep voltammetry (LSV) was performed in  $\text{N}_2$  and Ar-saturated electrolytes (Fig. 3a) to show the response current of electrochemical  $\text{N}_2$  reduction. It shows that the current in  $\text{N}_2$ -saturated electrolytes is higher than that in Ar-saturated electrolytes and suggests that  $\text{N}_2$  undergoes electrochemical reduction with the

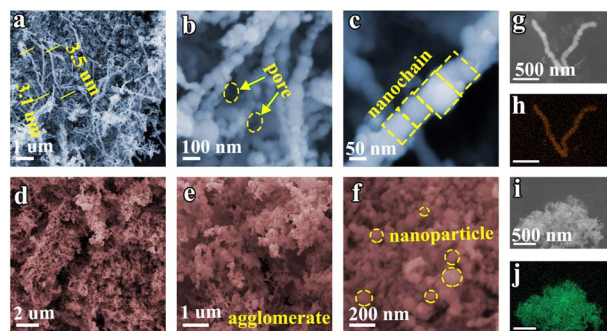


Fig. 1 SEM images of (a–c) Fe nanochains and (d–f) Fe nanoparticles. (g and h) Element mapping of Fe nanochains. (i and j) Element mapping of Fe nanoparticles.

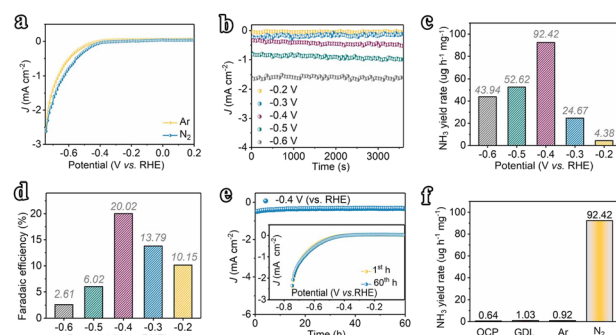


Fig. 3 (a) LSV curves of the Fe nanochain electrode recorded for  $\text{N}_2$  electro-fixation in  $\text{N}_2$ -saturated and Ar-saturated  $0.1 \text{ M Na}_2\text{SO}_4$  solution (scan rate  $5 \text{ mV s}^{-1}$ ). (b) Chronoamperometry curves of the Fe nanochain at  $-0.2$ – $0.6 \text{ V (vs. RHE)}$ . (c and d)  $\text{NH}_3$  yields and faradaic efficiencies of the Fe nanochain at  $-0.2$ – $0.6 \text{ V (vs. RHE)}$ . (e) Stability test for 60 h at  $-0.4 \text{ V (vs. RHE)}$ ; the inset of (e) shows LSVs of the electrode before and after the stability test. (f)  $\text{NH}_3$  yields of the Fe nanochain at  $-0.4 \text{ V (vs. RHE)}$  under different testing conditions.



Fe nanochain electrode. Furthermore, the currents at different potentials were examined to show the electro-reduction of  $N_2$  (Fig. 3b). From  $-0.2$  V vs. RHE to  $-0.6$  V vs. RHE, the corresponding currents increase up to about  $1.6$  mA cm $^{-2}$  at  $-0.6$  V vs. RHE. Generally,  $N_2$  is reduced to  $NH_3$  via the six-electron pathway or  $N_2H_4$  via the four-electron pathway through electrochemical fixation. Thus, the indophenol blue and Watt–Chrisp methods were applied to determine the finally generated products (Fig. S6–S10†). The resulting product  $NH_3$  was quantified. Corresponding with the increase of currents, from  $-0.2$  to  $-0.4$  V vs. RHE, the yield rate and faradaic efficiency of  $NH_3$  are gradually up to  $92.42$   $\mu$ g h $^{-1}$  mg $^{-1}$  and 20.02% (Fig. 3c and d). Nevertheless, the potential at  $-0.4$  V vs. RHE presents the highest yield rate and faradaic efficiency which is higher than the potential at  $-0.5$  V vs. RHE ( $52.62$   $\mu$ g h $^{-1}$  mg $^{-1}$  and 6.02%) and  $-0.6$  V vs. RHE ( $43.94$   $\mu$ g h $^{-1}$  mg $^{-1}$  and 2.61%). Therefore, compared to the state-of-the-art catalysts reported in the literature, our Fe nanowires are among the most outstanding NRR electrocatalysts disclosed to date (Table S1†). The stability of activity was examined using the current at  $-0.4$  V vs. RHE. As shown in Fig. 3e, any decrease of current is presented for 60 h at  $-0.4$  V vs. RHE and the LSV of the electrode after 60 h also suggests this result, which means the sustainable activity for electro reduction of  $N_2$  of this Fe nanochain. After the stability test, the XRD of the used Fe nanochain was used to characterize the crystal change (Fig. S11†). It presents a sharper peak ascribed to Fe of the used Fe nanochain than the fresh Fe nanochain. Additionally, the TEM images of the used Fe nanochains show that the nanochain structure remains intact after the stability test, with a more distinct interface between crystalline and amorphous regions. The observed lattice fringes can be attributed to the Fe (110) plane (Fig. S12†). This indicates that the amorphous Fe nanowires gradually crystallize during the electrocatalytic  $N_2$  reduction process. To trace the source of  $NH_3$ , the yields of  $NH_3$  were measured at the open-circuit potential and applying the gas diffusion electrode at  $-0.4$  V vs. RHE, suggesting almost no  $NH_3$  generation ( $0.64$   $\mu$ g h $^{-1}$  mg $^{-1}$  and  $1.03$   $\mu$ g h $^{-1}$  mg $^{-1}$ ) (Fig. 3f). Besides, the yield of  $NH_3$  applying Ar-saturated electrolyte is  $0.92$   $\mu$ g h $^{-1}$  mg $^{-1}$  but the  $N_2$ -saturated electrolyte exhibits  $92.42$   $\mu$ g h $^{-1}$  mg $^{-1}$  yield of  $NH_3$ . It shows that the  $NH_3$  results from the electroreduction of  $N_2$  in electrolyte, suggesting the high activity of the Fe nanochain for  $N_2$  electro-fixation.

Comparatively, the Fe nanoparticles are not assembled into nanochains and may not exhibit similar activity for  $N_2$  electro-fixation. The LSV of the Fe nanoparticle in Ar and  $N_2$  saturated electrolytes was measured (Fig. S13†). Almost few current responses are presented for electrocatalytic  $N_2$  reduction whereas high current densities are presented at different potentials (Fig. S14†). To accurately determine the generation of  $NH_3$  or not, the concentration of the produced  $NH_3$  was measured. As shown in Fig. 4a, the yield of  $NH_3$  of Fe nanoparticles is about  $32.82$   $\mu$ g h $^{-1}$  mg $^{-1}$  accompanied by 6.01% faradaic efficiency, which is far below that of the Fe nanochain (Fig. S15†). The total current densities of Fe nanochains and Fe nanoparticles at different potentials were examined to show the electrochemical activity. The Fe nanoparticle presents a higher total current density at  $-0.4$  V vs. RHE and  $-0.3$  V vs. RHE than the Fe nanochain

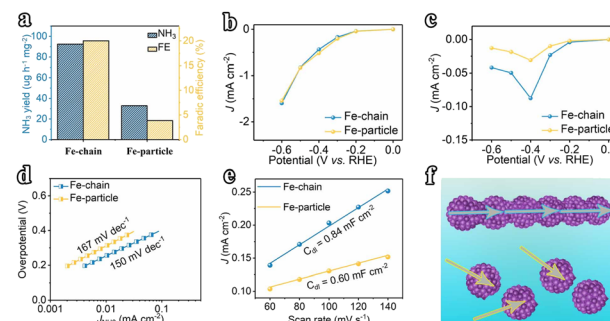


Fig. 4 (a)  $NH_3$  yields and faradaic efficiencies of Fe nanochains and Fe nanoparticles. (b) Current densities of Fe nanochains and Fe nanoparticles at  $-0.2$ – $0.6$  V (vs. RHE). (c) Partial current densities for  $N_2$  electroreduction at  $-0.2$ – $0.6$  V (vs. RHE). (d) Tafel slopes of Fe nanochains and Fe nanoparticles. (e) Capacitive plots of Fe nanochains and Fe nanoparticles at different scan rates (60–140 mV s $^{-1}$ ). (f) Schematic mechanism for promoting the electroreduction of  $N_2$ .

(Fig. 4b). However, the partial current densities for electrocatalytic  $N_2$  reduction are different between Fe nanochains and Fe nanoparticles (Fig. 4c), in which the difference at  $-0.4$  V vs. RHE is the greatest, also indicating the higher activity of Fe nanochains than Fe nanoparticles. This superior activity may be ascribed to the continuous electron transfer process of Fe nanochains. Thus, the Tafel slopes are used to explain the electron transfer rate. As presented in Fig. 4d, the Fe nanochain exhibits a lower Tafel slope than the Fe nanoparticle, suggesting a faster electron transfer process for  $N_2$  reduction. Furthermore, the Fe nanochain exhibits a larger  $0.85$  mF cm $^{-2}$  specific capacitance than the Fe nanoparticle ( $0.60$  mF cm $^{-2}$ ) (Fig. 4e and S16†), implying the larger electrochemical active surface,<sup>24–26</sup> which could contribute to the electrochemical performance of  $N_2$  reduction. Therefore, for Fe nanochains, several single amorphous Fe nanoparticles were stringed into nanochains which present more consecutive electron transfer than a single nanoparticle. This plays an important role in the multistep electron transfers of electrochemical  $N_2$  reduction and mainly promotes the corresponding performance of Fe nanochains.

## Conclusions

In conclusion, amorphous Fe nanoparticles were assembled into Fe nanochains via the magnetic-assisted method. This magnetic-assisted method exhibits the universality that assembles the magnetic Co and Ni nanoparticles into nanochains. The assembled Fe nanochain exhibits more excellent performance for electrochemical  $N_2$  reduction than the amorphous Fe nanoparticle. The Fe nanochain as the electrode for electrochemical  $N_2$  reduction takes full advantage of the exposed active sites of the single amorphous Fe nanoparticle and facilitates the continuous electron transfer process, which is important to the multistep electron transfer for the reduction of  $N_2$  to  $NH_3$ . This work adopts a novel method for assembling Fe nanoparticles into Fe nanochains and offers promising guidance for designing electrocatalysts.





## Data availability

The data supporting this article have been included as part of the ESI.†

## Author contributions

R. W. and J. L. conceived and designed the research; R. W. and J. L. synthesized the samples and performed the characterization; R. W., J. L., X. L. and C. S. carried out the electrochemical measurements. R. W. and J. L. discussed and all authors co-wrote the manuscript.

## Conflicts of interest

There are no conflicts to declare.

## Acknowledgements

This work was supported by the Research project of Chongqing Municipal Education Commission (KJQN202004501 and KJQN202304508).

## Notes and references

- 1 Y. Sun, W. Fan, Y. Li, N. L. D. Sui, Z. Zhu, Y. Zhou and J. M. Lee, *Adv. Mater.*, 2024, **36**, e2306687.
- 2 W. Qiu, X. Xie, J. Qiu, W. Fang, R. Liang, X. Ren, X. Ji, G. Cui, A. M. Asiri, G. Cui, B. Tang and X. Sun, *Nat. Commun.*, 2018, **9**, 3485.
- 3 Y. Sun, L. Yu, S. Xu, S. Xie, L. Jiang, J. Duan, J. Zhu and S. Chen, *Small*, 2022, **18**, 2106358.
- 4 C. Tang and S. Qiao, *Chem. Soc. Rev.*, 2019, **48**, 3166.
- 5 Y. Sun, X. Li, Z. Wang, L. Jiang, B. Mei, W. Fan, J. Wang, J. Zhu and J. M. Lee, *J. Am. Chem. Soc.*, 2024, **146**, 7752.
- 6 X. Zhao, G. Hu, G. Chen, H. Zhang, S. Zhang and H. Wang, *Adv. Mater.*, 2021, **33**, 2007650.
- 7 Y. Sun, W. Wu, L. Yu, S. Xu, Y. Zhang, L. Yu, B. Xia, S. Ding, M. Li, L. Jiang, J. Duan, J. Zhu and S. Chen, *Carbon Energy*, 2023, **5**, e263.
- 8 Y. Sun, S. Ding, B. Xia, J. Duan, M. Antonietti and S. Chen, *Angew. Chem., Int. Ed.*, 2022, **61**, e2021151.
- 9 Y. Sun, B. Xia and J. Duan, *J. Mater. Chem. A*, 2021, **9**, 20040.
- 10 X. Wu, L. Xia, Y. Wang, W. Lu, Q. Liu, X. Shi and X. Sun, *Small*, 2018, **14**, 1803111.
- 11 Y. Zhang, J. Zhao, D. Yang, B. Wang, Y. Zhou, J. Wang, H. Chen, T. Mei, S. Ye and J. Qu, *Nat. Chem.*, 2022, **14**, 46.
- 12 M. D. Walter, *Nat. Chem.*, 2021, **14**, 12.
- 13 A. McSkimming and D. L. M. Suess, *Nat. Chem.*, 2021, **13**, 666.
- 14 T. Wu, X. Zhu, Z. Xing, S. Mou, C. Li, Y. Qiao, Q. Liu, Y. Luo, X. Shi, Y. Zhang and X. Sun, *Angew. Chem., Int. Ed.*, 2019, **58**, 18449.
- 15 J. Duan, Y. Sun, S. Chen and C. Zhao, *J. Mater. Chem. A*, 2020, **8**, 18810.
- 16 Y. Sun, T. Jiang, J. Duan, L. Jiang, X. Hu, H. Zhao, J. Zhu, S. Chen and X. Wang, *ACS Catal.*, 2020, **10**, 11371.
- 17 B. Jiang, H. Xue, P. Wang, H. Du, Y. Kang, J. Zhao, S. Wang, W. Zhou, Z. Bian, H. Li, J. Henzie and Y. Yamauchi, *J. Am. Chem. Soc.*, 2023, **145**, 6079.
- 18 J. Kang, X. Chen, R. Si, X. Gao, S. Zhang, G. Teobaldi, A. Selloni, L. Liu and L. Guo, *Angew. Chem., Int. Ed.*, 2023, **62**, e2022174.
- 19 H. Yan, K. He, I. A. Samek, D. Jing, M. G. Nanda, P. C. Stair and J. M. Notestein, *Science*, 2021, **371**, 1257.
- 20 W. He, J. Zhang, S. Dieckhöfer, S. Varhade, A. C. Brix, A. Lielpetere, S. Seisel, J. R. C. Junqueira and W. Schuhmann, *Nat. Commun.*, 2022, **13**, 1129.
- 21 B. K. Mahato and A. Barman, *J. Mater. Sci.*, 2021, **56**, 19476.
- 22 Z. Wei, Y. Qiu, H. Chen, K. Yan, Z. Zhu, Q. Kuang and S. Yang, *J. Mater. Chem. A*, 2014, **2**, 5508.
- 23 S. Yu, D. Kim, Z. Qi, S. Louisia, Y. Li, G. A. Somorjai and P. Yang, *J. Am. Chem. Soc.*, 2021, **143**, 19919.
- 24 S. Cao, Y. Sun, S. Guo, Z. Guo, Y. Feng, S. Chen, H. Chen, S. Zhang and F. Jiang, *ACS Appl. Mater. Interfaces*, 2021, **13**, 40618.
- 25 Y. Sun, S. Ding, C. Zhang, J. Duan and S. Chen, *J. Mater. Chem. A*, 2021, **9**, 1603.
- 26 Y. Sun, M. Li, J. Duan, M. Antonietti and S. Chen, *Angew. Chem., Int. Ed.*, 2024, e202402678.

